Pore network model predictions of Darcy-scale multiphase flow heterogeneity validated by experiments

Christopher Zahasky[1,2], Samuel J. Jackson[1,3], Qingyang Lin[1], Samuel Krevor[1]

[1]Department of Earth Science and Engineering, Imperial College London, London, England
[2]Department of Geoscience, University of Wisconsin-Madison, Madison, WI, USA
[3]CSIRO Energy, Private Bag 10, Clayton South, Victoria 3169, Australia

Key Points:

- Pore network models extracted from X-ray micro-computed tomography scans can predict capillary heterogeneity in subdomains of core samples.
- Darcy-scale simulation results, parameterized with pore network model output, agree well with independent experimental measurements.
- A digital rocks approach is presented for multiphase characterization that requires no experimental calibration.

Corresponding author: Christopher Zahasky, chris.zahasky@gmail.com

Abstract

Small-scale heterogeneities in multiphase flow properties fundamentally control the flow of fluids from very small to very large scales in geologic systems. Inability to characterize these heterogeneities often limits numerical model descriptions and predictions of multiphase flow across scales. In this study, we evaluate the ability of pore network models (PNM) to characterize multiphase flow heterogeneity at the millimeter scale using X-ray micro-computed tomography images of centimeter-scale rock cores. Specifically, pore network model capillary pressure and relative permeability output is used to populate a Darcy-scale numerical model of the rock cores. These pore-network-derived Darcy-scale simulations lead to accurate predictions of core-average relative permeability, and water saturation, as validated by independent experimental datasets from the same cores and robust uncertainty analysis. Results highlight that heterogeneity in capillary pressure characteristics are more important for predicting local and upscaled flow behavior than heterogeneity in permeability or relative permeability. The leading uncertainty in core-average relative permeability is driven not by the image processing or PNM extraction, but rather by ambiguity in capillary pressure boundary condition definition in the Darcy scale simulator. This workflow enables characterization of local capillary heterogeneity and core-averaged multiphase flow properties while circumventing the need for the most complex experimental observations conventionally required to obtain these properties.

1 Keywords

digital rock physics, pore network model, capillary heterogeneity, X-ray computed tomography, multiphase flow, simulation

2 Plain Language Summary

To understand how fluids flow in subsurface rocks it is often necessary to perform laborious and expensive experiments aimed at replicating the subsurface pressure and temperature conditions. In this study, we propose and test a new modeling-based approach using high-resolution images capable of describing the structure and pore space of the rock at a resolution ten times smaller than the width of a typical human hair. We show that with these high-resolution images, along with a few routine rock property measurements, it is possible to predict the distribution of fluids in the rocks at range of subsurface fluid flow conditions. This digital, or experiment-free, approach has the potential to redefine how we parameterize larger-scale models of problems such as contaminant flow in aquifers or carbon dioxide migration and trapping in carbon capture and storage reservoirs.

3 Introduction

Multiscale heterogeneity, intrinsic to permeable geologic media, dictates single and multiphase fluid flow across a range of applications in hydrogeology and subsurface energy resource development (P. S. Ringrose et al., 1993; Feehley et al., 2000; Kang et al., 2017; Reynolds et al., 2018; Cowton et al., 2018). The reservoir-scale impacts of heterogeneous features below the resolution of typical reservoir model grid blocks lead to major challenges in predicting and history matching CO_2 storage and non-aqueous phase liquid migration in the subsurface (P. Ringrose et al., 2009; V. Singh et al., 2010; Eiken et al., 2011). Inability to characterize multiscale heterogeneity limits the predictive ability of existing digital rock approaches (Guice et al., 2014).

Advances in high-resolution X-ray micro-computed tomography (micro-CT) have enabled new methods for quantifying single and multiphase fluid flow at the pore scale. Micro-CT has been a valuable tool for experimental characterization of pore space geometry, (Lin et al., 2016) mineralogy (Lai et al., 2015; Menke et al., 2015; Beckingham et al., 2017; Al-Khulaifi et al., 2019), wettability (Iglauer et al., 2012; Bartels et al., 2019; Lin et al., 2019), residual trapping (Herring et al., 2013; Chaudhary et al., 2013; Al-Menhali & Krevor, 2016; Øren et al., 2019), and curvature-based capillary pressure (Armstrong et al., 2012; Herring et al., 2017; Garing et al., 2017; Lin et al., 2018; T. Li et al., 2018). Increased availability of affordable high-power computational and data management resources have enabled micro-CT imaging to increasingly be used to image centimeter-scale samples with voxel resolutions less than 10 micrometers (Lin et al., 2018; Jackson et al., 2019; Øren et al., 2019).

Models to describe fluid flow at the pore scale can be roughly categorized as direct simulation methods and pore network methods. In direct simulation methods, the Navier-Stokes equations are solved on a grid defined by the pore structure of the sample using approaches such as volume-of-fluid, level-sets, or Lattice-Boltzmann methods (Raeini et al., 2015). Alternatively, pore network models (PNM) approximate the pore-space as a construction of optimal shapes–such as balls and tubes–and use continuum solutions of the Navier-Stokes equation to describe fluid flow. By using Navier-Stokes continuum approximations of fluid flow in the pore space, pore network models are able to achieve orders of magnitude faster computational times than direct simulation methods (Raeini et al., 2015; Bultreys et al., 2016; Zhao et al., 2019), and therefore have the potential to run centimeter-scale sample domains. Pore network models have been used to study an array of processes in porous media such as solute and reactive transport (Bijeljic et al., 2004; Mehmani & Tchelepi, 2017), multiphase displacement behavior (Chen & Wilkinson, 1985; Lenormand et al., 1988; Idowu & Blunt, 2010; J. Li et al., 2017), diffusion-driven transport (De Chalendar et al., 2018), capillary pressure characteristic behavior (Bakke & Øren, 1997; Vogel et al., 2005; Silin & Patzek, 2006; Hussain et al., 2014), and relative permeability (M. Blunt & King, 1991; Jerauld & Salter, 1990; M. J. Blunt, 1997; Rajaram et al., 1997; Nguyen et al., 2006; Sheng & Thompson, 2016; Berg et al., 2016). However, computation and experimental complexity has limited multiphase PNM testing and validation to synthetic models (Hilpert & Miller, 2001), millimeter-scale experimental samples, or partial sample analysis (Guice et al., 2014). As a result, the ability for pore network models to describe and predict Darcy-scale multiphase flow heterogeneity has not yet been tested or validated against experimental measurements in centimeter-scale cores.

One of the biggest challenges with modeling natural systems at any scale is the uncertainty that arises from measurements, characterization, and mathematical descriptions of complex systems (Pianosi et al., 2016). When using pore network modeling to describe fluid flow in porous media, uncertainty arises in experimental observations (Bultreys et al., 2018), image resolution and processing (Arns et al., 2001; Wildenschild & Sheppard, 2013; Leu et al., 2014; Berg et al., 2018; A. Singh et al., 2018), network extraction and descriptions (Joekar-Niasar et al., 2010; Dong & Blunt, 2009; Lindquist et al., 2004; Jiang et al., 2007; Mehmani & Tchelepi, 2017), and flow modeling or characteristic curve development (Silin & Patzek, 2006). Current methods to characterize multiscale multiphase heterogeneity in geologic systems are often nonunique, expensive, laborious, and require restricting assumptions (Reynolds & Krevor, 2015; Zahasky & Benson, 2018). The resulting experimental and modeling uncertainty has often restricted workflows to tuning pore network or continuum scale models to experimental results, thus limiting their predictive ability.

In this study, we describe an approach for building heterogeneous multiphase Darcy-scale models of centimeter-scale cores utilizing pore network model predictions of characteristic curves in representative elementary volume (REV) subdomains. The approach of using pore network models to characterize heterogeneity in REV subdomains, rather than entire samples, is intrinsically parallelizable and scalable to larger sample sizes. Uncertainty analysis is used to demonstrate that the capillary heterogeneity is greater than the uncertainty in pore network model capillary entry pressure that arises from variations in image processing. This approach utilizes only published contact angle and interfacial tension data, mercury injection capillary pressure (MICP) curves, and dry micro-CT scans for pore network model (PNM) extraction and flow. Comparing Darcy-scale fluid saturation results of this hybrid modeling approach with experimentally measured fluid saturations during multiphase drainage experiments in the same cores provides an independent means to test the predictive ability of the pore network models to describe Darcy-scale flow heterogeneity. This approach, combined with robust sensitivity analysis, provides a foundation for future multiscale, multiphase characterization of geologic porous media without the need for the most laborious and expensive components of traditional multiphase flow characterization.

4 Methods

4.1 Overview

The key data required to build and test the workflow in this study—summarized in Figure 1—are high resolution X-ray micro-computed tomography images of two different core samples acquired by Jackson et al. (2019) (Section 4.2). Dry scans are used to describe the pore-scale geometry of centimeter-scale Bentheimer sandstone cores (*Dry Scan* plot in Figure 1). Bentheimer was selected for this study because of its stability and large pore size. One sample had subtle heterogeneity, while the other sample had clear sedimentary laminations oriented obliquely to the axis of the core.

The first step in the workflow was to discretize the dry scan images into representative elementary volume (REV) sized subdomains and segment the subdomain images to calculate Darcy-scale porosity (*Porosity* plot in Figure 1) (Section 4.4.3). This discretization enabled unlimited parallelization of the proposed workflow in this study and reduced the computational burden of working with large datasets. The dry micro-CT image sizes of the full samples used in this study were over 60 GB each. Segmented subdomain blocks from the dry scan were run through a pore network model to estimate capillary entry pressure (*Entry Pressure* plot in Figure 1) and relative permeability. The PNM-derived capillary pressure curves are used to define the local capillary entry pressure. These entry pressure values are then used to locally scale the mercury injection capillary pressure curve. This enables capillary pressure to be characterized in sub-resolution pores in the sample. The resulting capillary pressure curve, porosity, and PNM-derived relative permeability curves in each subdomain were then used to parameterize each grid cell of a Darcy-scale numerical model.

To assess the validity of pore network model multiphase characteristic curve predictions, fluid saturation simulation output from the Darcy-scale model (*Simulation* S_w in Figure 1) is compared with experimentally measured fluid saturations at equivalent flow rate conditions (Section 4.5). Micro-CT scans at a range of fraction flow conditions (*Water FF:0* example shown in Figure 1) are used to calculate local Darcy-scale fluid saturations in discrete subdomains of the cores (*Experimental* S_w plot in Figure 1). This independent comparison between experimentally measured water saturation, and numerically simulated water saturation in equivalent subdomains provides a means to evaluate the predictive ability of uncalibrated pore network models to describe Darcy-scale multiphase flow behavior.

4.2 Core Samples and Experiment Description

Two Bentheimer cores were utilized in this study. The first, a relatively homogeneous core (hereafter referred to as Core 1), was 1.24 cm in diameter and 7.32 cm long. A second core was selected because it had clear sedimentary lamination, providing the opportunity to study layered heterogeneities (hereafter referred to as Core 2). Core 2 was 1.24 cm in diameter and 6.47 cm long. The micro-CT image acquisition and multiphase flow experiments are described in detail in Jackson et al. (2019). Briefly, the cores were first loaded into a custom fabricated PEEK coreholder with stainless steel end caps. A Zeiss Versa 510 CT scanner was used to acquire dry scans of nearly the entire volume of each core with 6 μm cubic voxel side length. Imaging artifacts arising from the stainless steel coreholder end caps limited the scan length of the Core 1 to 6.48 cm and the scan length of Core 2 to 5.69 cm. To acquire micro-CT datasets 6.48 and 5.69 cm in total length, 12 and 10 separate scans were taken in the Core 1 and 2, respectively. Fol-

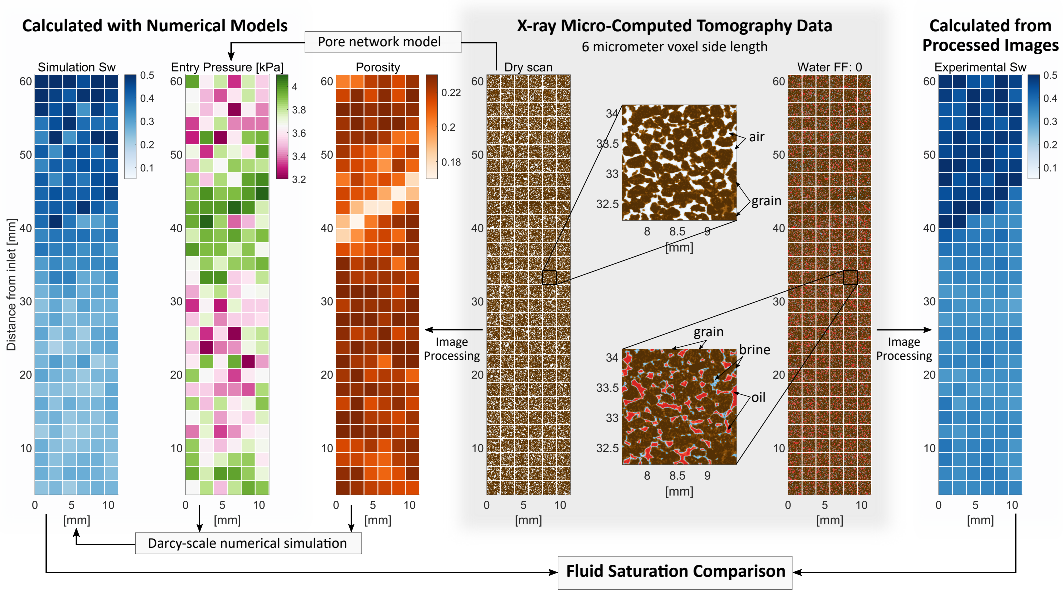

Figure 1. A methodological overview and illustration of the data set for Core 2 utilized in this study. The gray shaded region highlights center-slice micro-CT scans along the axis of the core during dry and drainage multiphase flow at a water fractional flow equal to zero. To the left of the micro-CT data is the resulting Darcy-scale porosity (from image processing), capillary entry pressure (from PNM), and simulated water saturation (S_w). To the right of the micro-CT data is the Darcy-scale water saturation calculated from image processing of the multiphase micro-CT data at the same water fraction flow. In the experiments and models fluid is injected from bottom to top.

lowing the completion of dry scans, the cores were saturated with doped brine (3.5 weight percent potassium iodide) such that the drainage experiments started at fully water saturated conditions ($S_w = 1$). The core-averaged permeability was measured from multiple single-phase flow rates and found to be 1635 mD and 763 mD in Core 1 and 2, respectively. Steady-state co-injection of brine and decane was performed at water fractional flows (FF) of 0.95 and 0 in Core 1, and 0.95, 0.5, and 0 in Core 2. The fluids were injected from the bottom of the vertically oriented coreholder mounted in the micro-CT scanner. Scan time and data management considerations prevented experimental measurements at additional fractional flow increments in Core 1. The total flow rate in all experiments was 0.1 mL/min. Decane was used as the nonwetting phase fluid to minimize the density contrast with water. In addition, the higher viscosity of decane relative to gaseous nonwetting phases maximizes fluid stability during the multi-hour X-ray micro-CT scans (Reynolds et al., 2017). Once the differential pressure stabilized at each fractional flow, a scan was taken of nearly the entire core with a 6 μm cubic voxel size.

4.3 Full-core Image Reconstruction

Image reconstruction was first performed with the Zeiss reconstruction software to correct for beam-hardening and center-shift artifacts. Following reconstruction, the multi-scan images were re-normalized, registered, merged, and cropped using the workflow described in detail in Jackson et al. (2019). This workflow produced a raw 16-bit grayscale micro-CT image of each core during the dry and multiphase scans. The final image sizes were $950 \times 950 \times 10,800$ voxels (76.4 GB) and $954 \times 954 \times 9,540$ voxels (64.1 GB) in Core 1 and Core 2, respectively.

4.4 Image Processing and Pore Network Modeling

4.4.1 Pore Network Modeling and Network Extraction

An array of pore network extraction and simulation options are available for a growing range of pore-scale applications. In this study the maximal ball method described by Dong and Blunt (2009) is utilized with the free, open-source network extraction algorithm (PNextract) developed by Raeini, Bijeljic, and Blunt (2017). As implemented, no assumptions are made about the topology of the network. Features such as coordination number and throat geometry are calculated automatically and have been previously validated (Dong & Blunt, 2009), the pores are approximated as spheres.

The pore network model simulations were run using the approach of Valvatne and Blunt (2004) with the updated algorithm (PNflow) described in Raeini, Bijeljic, and Blunt (2018) and further validated by Bultreys et al. (2018) and Raeini et al. (2019). This model relies on an assumption of quasi-static capillary dominated flow. Capillary pressure during drainage is based on fluid interface force balances using the Mayer-Stowe-Princen method (Mason & Morrow, 1991). See references for additional details of model extraction and formulation. Details of parameter settings can be found in examples given in the data repository referenced in the Acknowledgements.

4.4.2 Impact of Image Processing Uncertainty on Pore Network Model Output

To establish a pore network modeling workflow that is as insulated from user subjectivity as possible, a robust image processing uncertainty analysis was performed on a subdomain ($333 \times 333 \times 333$ voxels $= 2 \times 2 \times 2$ mm) of Core 1. The main sources of uncertainty can be categorized as image acquisition, image processing, pore network extraction, and pore network simulation parameterization. The output function used to evaluate uncertainty was the pore network model drainage capillary pressure curve. Initial screening sensitivity of various segmentation methods, network extraction input, pore network simulation variables found that image processing had by far the greatest impact on this characteristic curve output relative to the other categories tested, and therefore was the focus of the uncertainty analysis. Different acquisition settings were not tested as these will be highly dependent on different micro-CT scanner hardware. While contact angle and interfacial tension are very important parameters in the network model simulation, these properties were well constrained from previous experimental studies with similar rock-fluid pairs (Lin et al., 2018; Jackson et al., 2019). For other rock-fluid pairs, there are extensive contact angle and interfacial tension datasets available in literature (e.g. Kazakov et al. (2012); Ethington (1990); Espinoza and Santamarina (2010)), however this is an active area of research.

The three main steps in a typical image processing workflow are filtering/denoising, edge sharpening, and segmentation (i.e. the conversion of a grayscale image into a image with voxels categorized as air-rock in the dry scan, or water-decane-rock in the multiphase flow scans). The filter methods tested were the Median 3D filter, the Non-local Means Denoising (Buades et al., 2005), and the Gaussian Blur 3D. Realizations either had no edge sharpening or used the Unsharpen Mask ImageJ plugin. The image segmentation algorithms tested included the Robust Automatic Threshold (RATS), the Otsu method, Statistical Region Merging, and a global threshold. The massive size of the experimental datasets that needed to be efficiently processed prevented the use of more computationally expensive and sophisticated segmentation tools such as Weka or other machine-learning based methods. All image processing was completed in the open-source image analysis/processing software FIJI/ImageJ.

To provide a robust analysis and extensive survey of the image processing parameter space (i.e. the range of reasonable values for each image processing method), an automated routine was written in Matlab to interface with FIJI via MIJ (Sage et al., 2012). A nested sampling routine was used for mapping the image processing input of 1000 processed image realizations. An Excel sheet with specific parameter input ranges of each method is included in the Supporting Information (SI).

Following the segmentation of each realization, an automated post-processing examination was performed to reject unphysical realizations. This examination was performed by sampling a small subregion of the image confidently, approximately 50 voxels by 50 voxels, known to be solid grain. If the segmented image contained any pore space in this subregion then the realization was rejected. The remaining 557 realizations were run through PNextract and PNflow by calling the executables from Matlab. All realizations were run with identical extraction and flow settings. Of the resulting models, 373 remained after a final screening that rejected models with an average porosity in the REV-scale subregion outside of the range of 0.17-0.221. This range was chosen based on a core-average medical CT porosity measurement that uses linear scaling of dry and fully water saturated sample scans for Core 1 (Akin & Kovscek, 2003). This provides an independent measurement of porosity with medical CT as opposed to thresholding dry micro-CT scans. A schematic overview of the analysis performed is provided in Figure 2. The first slice of seven example segmented realizations are shown in Figure S1 in the SI. The first ten realizations, pore network input and output files, and Matlab scripts for method automation and pore network model interfacing are included in the data repository referenced in the Acknowledgements.

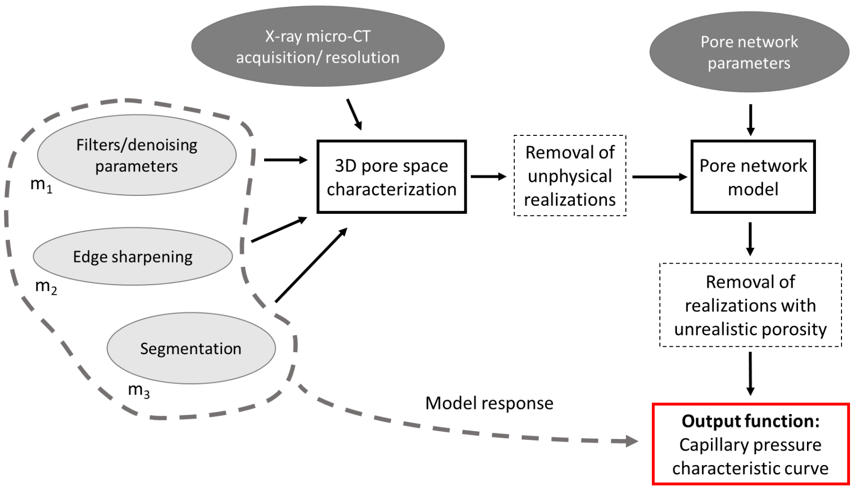

Figure 2. Schematic overview of image processing uncertainty workflow. Dark ovals indicate parameters tested with scoping sensitivity studies, the light gray ovals indicate parameters extensively evaluated by sampling from parameter distribution functions. This workflow was used to generate 1000 processed and segmented 3D image realizations of a single subvolume of Core 1. After the realization rejection steps, as indicated by dashed rectangular boxes, 373 capillary pressure curves were produced. Figure S2 in the SI illustrates the capillary pressure and relative permeability of these 373 models.

4.4.3 Image Processing Workflow

Based on the sensitivity analysis results (provided in Figure S2 in the SI), the image processing and pore network modeling workflows written in Matlab were adapted to process the entire datasets for each Bentheimer core. The workflow for the dry micro-CT data was as follows:

1. Raw normalized, merged, micro-CT images were filtered with the ImageJ Non-local Means Denoising.
2. Filtered images were segmented into air/rock binary images (e.g. top zoomed image in Figure 1). Segmentation was performed with a global threshold in ImageJ chosen such that the porosity at the inlet of the core was equal to the independent porosity measurement. This segmentation approach often leads to over-segmentation due to the compensation for sub-resolution porosity. As noted in previous studies, this can have dramatic impacts on permeability prediction (Berg et al., 2018), however the sensitivity analysis in this study indicates that this over-segmentation has a limited impact on capillary entry pressure measurement. In this study we used a single measurement of effective porosity at the inlet of the cores taken from medical CT porosity measurements. Medical CT porosity measurements provide effective porosity measurements along the length of the core by performing linear scaling between dry scans and fully saturated scans (Akin & Kovscek, 2003). Analogous independent effective porosity measurements could utilize Helium pycnometery or other measurement techniques on adjacent samples to the core. In the Bentheimer cores nearly all of the porosity is connected, however in other samples the extent of connected and unconnected porosity may determine the measurement technique used to threshold the dry scans.
3. Segmented images were discretized into separate smaller REV-scale 3D subdomains. The subdomains were $316 \times 316 \times 300$ and $316 \times 316 \times 318$ voxels in Core 1 and 2, respectively. This corresponded to an approximately cubic pore network model and Darcy-model grid cell size with a side length equal to 1.896mm (6μm$\times$316 voxels). The subdomain sizes are slightly different in the direction parallel to the axis of the core due to the different lengths of the cores. The REV side-length dimensions were determined from detailed REV analysis performed by Jackson et al. (2019) and are in agreement with previous Bentheimer REV analysis (Halisch, 2013).

4. The porosity of the discretized subdomains was calculated by $\phi_i = \varphi_{air,i}/\varphi_{rock,i}$. Here $\varphi_{air,i}$ is the volume fraction segmented as air, and $\varphi_{rock,i}$ is the volume fraction segmented as rock.
5. Pore networks were extracted with PNextract from each subdomain segmented image.
6. Pore network model flow simulations were run on the extracted subdomains with PNflow.

Using a similar workflow, it was possible to measure local water saturation in the discretized subdomains for comparison with Darcy-scale model simulation output. The image processing workflow for the multiphase flow experiments was as follows:

1. Raw normalized, merged, micro-CT images were filtered with the ImageJ non-local means filter.
2. Filtered images were segmented into nonwetting phase/brine+rock binary images with a global threshold. The segmentation threshold value was determined from the minimum histogram value between the nonwetting phase (decane) and brine histogram peaks. This is illustrated in Figure S3 in the Supporting Information.
3. Segmented images were discretized into smaller subdomains identical in size to the dry scan discretization.
4. The water saturation of each subdomain i was calculated by $S_{w,i} = (1-(\varphi_{nw,i}/\phi_i))$. Here $\varphi_{nw,i}$ is the volume fraction of nonwetting phase in the subdomain.

Water saturation measurement uncertainty was estimated by calculating subdomain water saturation on images segmented at thresholds plus and minus 5% of the grayscale range relative to the histogram minimum established in step 2 (see histogram illustration in Figure S3 of the SI). Porosity, raw PNM output, and characteristic curve fits for every subdomain of both rocks are provided in the data repository referenced in the Acknowledgements.

4.5 Darcy-Scale Modeling

Darcy-scale multiphase simulation was performed with the Computer Modeling Group (CMG) IMEX commercial reservoir simulator (Computer Modelling Group LTD, 2017).

The grid cell discretization was set to exactly match the processed image and pore-network model dimensions (e.g. see saturation maps in Figure 1).

Four sets of simulations were run on each core. These were designed to test the relative importance of including heterogeneity in capillary pressure and relative permeability characteristics, as derived from the pore network models. The first set of simulations utilized a constant set of capillary pressure and relative permeability curves in every grid cell—excluding the end slices, as described below. These models show the fluid saturation distribution assuming the cores behave as homogeneous porous mediums. The second set of simulations used PNM-derived capillary pressure and relative permeability curves to parameterize the characteristic heterogeneity throughout the cores. These models highlight the improved match between modeled saturation distribution and the experimental data when heterogeneity is characterized. The third set of simulations used PNM-derived capillary pressure and a single relative permeability curve determined from the mean of the PNM output to parameterize the characteristic heterogeneity throughout the cores. These models demonstrate the limited influence of relative permeability characterization on fluid saturation distribution. The final set of simulations used the same heterogeneous characteristic curves but had a constant permeability value of 1000 mD in both cores, rather than using the experimentally measured permeability of 1635 mD and 763 mD in Core 1 and 2, respectively. These models emphasize that exact experimental permeability measurements are not necessary to implement the workflow described here.

In the homogeneous simulation models, the relative permeability curves were taken from previous experimental measurements on large core samples by Jackson et al. (2019) and Reynolds and Krevor (2015) (dashed black lines in Figure 3). These wetting and nonwetting phase relative permeability functions from previous work are defined by the modified Brooks-Corey functions $k_{rw} = ((S_w - S_{wir})/(1 - S_{wir}))^{4.4}$ and $k_{rnw} = k_{rnw,ir}(1 - (S_w - S_{w,ir})/(1 - S_{w,ir}))^{4.6}$, respectively. The nonwetting phase relative permeability at the irreducible water saturation is $k_{rnw,ir} = 0.8$. The irreducible water saturation is $S_{w,ir} = 0.08$ (Jackson et al., 2019; Reynolds & Krevor, 2015). The homogeneous model capillary pressure curve was derived from the fluid-scaled MICP curve, represented by the yellow line shown in Figure 4.

In the heterogeneous models of Core 1 and Core 2 pore network model output is used to define the capillary pressure and relative permeability of each grid cell. Based on the uncertainty analysis—and as observed by previous studies—the capillary pressure in the smallest pores at low wetting phase saturation has the highest uncertainty (Silin & Patzek, 2006; Berg et al., 2016). The most accurate portion of the pore network model capillary pressure prediction is at high water saturations (i.e. largest features in the micro-CT images). Therefore, the raw pore network model capillary pressure values from $S_w = 0.8$ to $S_w = 0.9$ were used to scale the MICP curve via a linear least squares fitting method implemented in Matlab. The portion of the capillary pressure curve from $S_w = 0.9$ to $S_w = 1$ was not used for fitting because this portion of the curve is dependent on boundary conditions and pore network extraction definition. These boundary effects were found to decrease with increasing model/subdomain size, in agreement with previous modeling (Papafotiou et al., 2008; Raeini et al., 2019) and experimental studies (Norton & Knapp, 1977; Zahasky et al., 2018). This approach of scaling the MICP capillary pressure is similar to other approaches that use porosity/permeability/saturation relationships to scale local capillary entry pressure to define capillary heterogeneity (Krevor et al., 2011; Krause, 2012; B. Li & Benson, 2015). The raw and scaled capillary pressure curve for every grid cell in Core 2 are shown in Figure 4. The heterogeneous relative permeability curves were defined by modified Brooks-Corey relative permeability curves fit to PNM output. A plot of the raw and fitted PNM relative permeability output for every subdomain in both cores is shown in Figure 3.

In all models the grid cell porosity was heterogeneous and determined directly from the segmented micro-CT image of the corresponding subdomain (i.e. step 4 of the dry image workflow described above). To parameterize the model inlet and outlet face conditions, three inlet slices and three outlet slices were added to the portion of the models defined by the scanned section of the cores. In all models, the first and last slices were set to replicate the experimental coreholder inlet and outlet caps. These had linear relative permeability curves, permeability set an order of magnitude higher than the respective core matrix permeability, and a constant capillary pressure of 0.2 kPa. Results of 0 kPa and 3.7 kPa capillary pressure were also tested to illustrate the impact of the capillary end effect on the relative permeability uncertainty as shown in Figure 3. A capillary pressure of 0.2 kPa was used because this is the theoretical capillary pressure of the tubing entering and exiting the coreholder in the experiments. The tubing outer di-

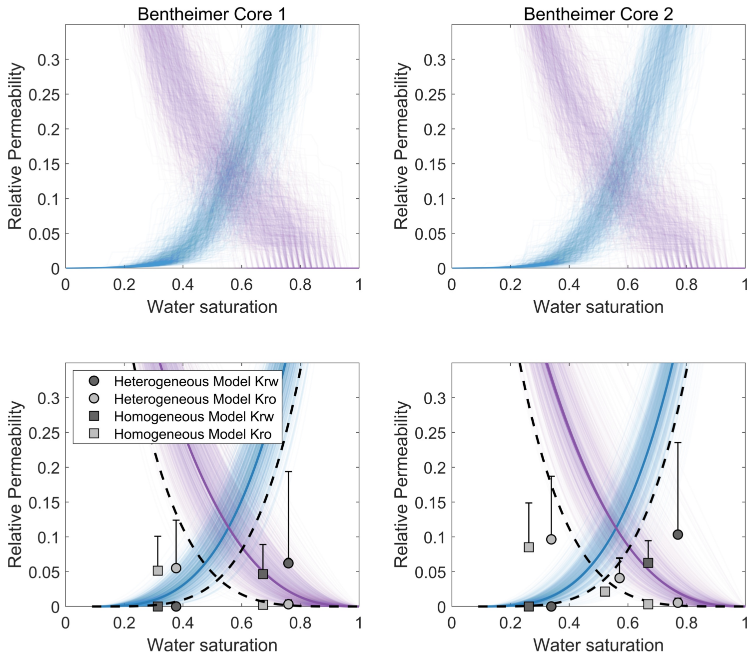

Figure 3. Raw pore network model relative permeability curves (top plots) and modified Brooks-Corey relative permeability functions fit to the raw output (bottom plots). The plots on the left illustrate the relative permeability in every subdomain in Core 1, while the plots on the right are for every subdomain in Core 2. The blue lines indicate water relative permeability (k_{rw}) and the purple lines indicate oil relative permeability (k_{ro}). The bold lines in the bottom plots illustrate the average modified Brooks-Corey relative permeability of all of the PNM output. The dashed black lines define the modified Brooks-Corey relative permeability in the homogeneous simulation models and are based on experimental measurements in a number of Bentheimer samples from previous studies (Jackson et al., 2019; Reynolds & Krevor, 2015). The square points in the bottom plots indicate core-average relative permeability calculated in the fully homogeneous CMG simulation model. The circular points in the bottom plots show the core-average relative permeability calculated from the fully heterogeneous CMG simulation model results. The vertical error bars on the simulation points illustrates the dominant impact of the boundary conditions on uncertainty in the estimate of pressure differential. Specifically, the vertical bar above the symbols in Figure show the change in core-average relative permeability when the inlet and outlet slice capillary pressure is set to 3.7 kPa rather than 0.2 kPa (plotted points). The lower error bars are smaller than the symbol size indicating that there is little different when the inlet and outlet capillary pressure is 0 kPa rather than 0.2 kPa. The outlet slice capillary pressure has less influence on the core-average saturation measurements; the saturation variation is smaller than the size of the data markers.

ameter was 1.5875 mm and the inner diameter was 0.7938 mm. A capillary pressure of 3.7 kPa was chosen as an upper bounds because this is the average capillary entry pressure based on MICP analysis. Two additional slices were added to each end of the model to represent the unscanned portion of the core in the experiments. The relative permeability and capillary pressure curves in the unscanned slices were set to the average of the first and last model slices in the respective models. The full CMG model input and output files for both of the cores are available in the data repository referenced in the Acknowledgements.

5 Results

5.1 Pore Network Model Prediction of Capillary Heterogeneity

Core 2 was used for capillary heterogeneity analysis because dry image characterization indicated the presence of a low porosity zone crosscutting the sample near the outlet end of the core. This feature is illustrated in Figure 1 as the low porosity zone in the porosity map plot. The raw and scaled pore network model capillary pressure curves of every subdomain in Core 2 are shown in Figure 4. The capillary pressure curves corresponding to the low porosity capillary barrier are highlighted in green. The elevated capillary entry pressure predicted in this zone by the PNM is qualitatively confirmed by the experimental saturation measurements (Figure 1 *Experimental* S_w plot). The measured saturation values indicate that this low porosity zone produced a capillary barrier that limited the invasion of nonwetting phase relative to the inlet of the core.

To confidently predict the capillary heterogeneity in porous media, the heterogeneity must be greater than the uncertainty in image processing and fluid saturation measurements. A comparison between the uncertainty analysis results and the PNM capillary heterogeneity is indicated by the red boxplot on the center plot, and zoomed inset to the right, in Figure 4. This comparison illustrates that the capillary pressure in nearly all the subdomains of the low porosity/capillary barrier zone in Core 2 (green lines) fall well above the bounds of uncertainty. This highlights that one of the key features necessary to predict and accurately simulate multiphase flow—capillary heterogeneity—can be determined with this pore network modeling workflow.

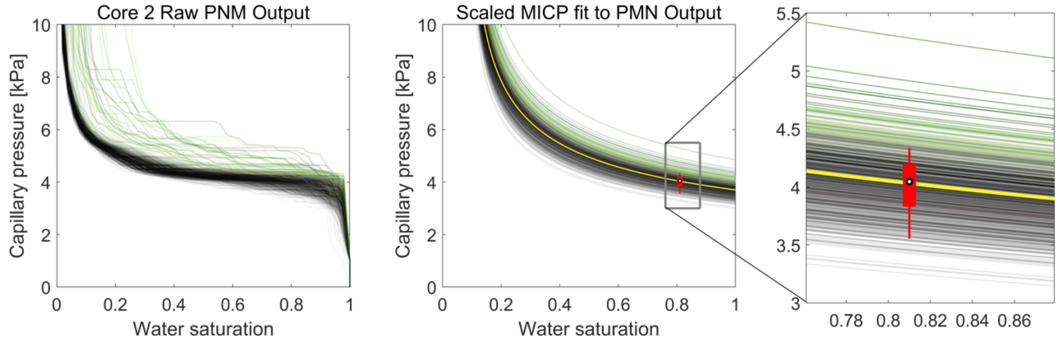

Figure 4. (left) Example raw capillary pressure curve output (both green and black lines) from every subdomain of Core 2. (middle) Corresponding capillary pressure curves used for every grid cell in the CMG model based on scaling the MICP curve (yellow line) based on curve fitting described in Section 4.5. (right) A zoomed-in plot of the scaled MICP curves. The green lines highlight the capillary pressure curves corresponding to the low porosity/high entry pressure zone visible in Figure 1. Specifically, the subdomains with a porosity less than 20% are colored in green. For reference, the shade of green corresponds to the entry pressure colorbar in Figure 1. The red box plot marks the range of uncertainty arising from the image processing workflow. The top and bottom of the thin red line indicate the 90th and 10th percentile results, found to be 3.56 kPa and 4.34 kPa, respectively. The top and bottom of the thick red line indicate the 75th and 25th percentile results, found to be 3.83 kPa and 4.20 kPa, respectively. The dot in the middle is the median capillary pressure (4.05 kPa) determined from the uncertainty analysis. A plot showing all of the raw capillary pressure curves used to calculate these statistics is shown in Figure S2 in the SI.

5.2 Improvement in Darcy-Scale Model When Accounting for Capillary Heterogeneity

A comparison between the experimentally measured water saturation and the water saturation from the CMG models is given for both cores in the right plots in Figure 5. The slice average comparisons include both the results of the CMG simulation with heterogeneous grid cell capillary pressure and relative permeability (bold solid lines), and homogeneous characteristic curves (thin solid lines). The local saturation variation in the experimental data decrease at lower water fractional flow as the impact of subtle differences in capillary forces are suppressed. However, the experimental saturation measurement uncertainty (shaded gray region around dashed lines) increases with decreasing water saturation. This happens because the nonwetting phase interfaces are the main source of segmentation uncertainty. Therefore, the saturation measurement uncertainty increases as the nonwetting phase interfacial area and nonwetting phase saturation increase.

The left plots in Figure 5 provide a direct comparison between micro-CT subdomain saturation and simulated saturations in every grid cell in the heterogeneous models. The scatter in the data is a reflection local differences in saturation between the model and the experimental measurements. This scatter is an accumulation of measurement error, thresholding uncertainty, and local model parameterization error. To more quantitatively compare the results of the CMG model saturation in every grid cell ($S_{w,n}^{sim}$) to the experimental water saturation in the corresponding subdomain ($S_{w,n}^{exp}$), the mean relative saturation error ($\bar{\delta}_{Sw}$) in every subdomain/grid cell (n) and at all fractional flows was calculated with Equation 1.

$$\bar{\delta}_{Sw} = \frac{1}{n}\sum_{n} \frac{|S_{w,n}^{exp} - S_{w,n}^{sim}|}{S_{w,n}^{exp}} \tag{1}$$

The mean grid cell relative saturation error for the homogeneous Core 1 CMG model at all fractional flows was 0.173 while the heterogeneous model using PNM input was 0.138. In the more heterogeneous Core 2, the homogeneous simulation model relative saturation error was 0.203 while the heterogeneous model was only 0.139. The improved saturation prediction in the heterogeneous models is due to a combination of more accurate local saturation prediction (e.g. the elevated water saturation behind the capillary barrier in Core 2) and the overestimation of nonwetting phase saturation in the homogeneous models in both cores.

To further highlight the importance of capillary heterogeneity, Figure 6 compares the results of the fully heterogeneous model shown in Figure 5 with the simulation model that uses the same heterogeneous PNM capillary pressure curves but only a single relative permeability curve. The single relative permeability curve is determined by taking the average of the PNM relative permeability curves in the respective cores (bold colored lines in lower plots in Figure 3). The slice-average saturation profiles from the models with homogeneous and heterogeneous relative permeability are nearly indistinguishable in Figure 6. This highlights that the capillary pressure heterogeneity characterization is essential in systems where capillary forces dominate over viscous forces. In contrast, heterogeneity in relative permeability characteristics contribute relatively little. This is likely due to the spatial character of the heterogeneity. In the cores in this study, the heterogeneity in capillary pressure characteristics is structured in layers (e.g. capillary entry pressure map in Figure 1) while the heterogeneity in relative permeability is unstructured.

Both cores show a capillary end effect, particularly at low fractional flows of water. The capillary end effect describes the elevated water saturation near the outlet of the cores driven by a capillary pressure discontinuity at outlet face. The end effect is slightly stronger in Core 2 due to the capillary barrier described above. The simulated core-average relative permeability values are shown in Figure 3. As illustrated by the vertical error bars, the core-average relative permeability in the models is strongly influenced by the simulation parameterization approach to account for the capillary end effect. The vertical bars in Figure 3 show the change in core-average relative permeability when the inlet and outlet slice capillary pressure is set to 3.7 kPa rather than 0.2 kPa. The core-average relative permeability in the homogeneous model (square points in Figure 3) are lower than the local grid cell input (dashed black lines) at all fractional flow rates because of the capillary end effect reduces the fluid mobility near the outlet of the core, particularly in the unscanned region. Despite the uncertainty in the core-average relative permeability, the PNM subdomain relative permeability predictions are systematically higher than the bulk experimental measurements. The implementation of these subdomain measurements in the heterogeneous models leads to core-average simulation relative permeability values (circular points in Figure 3) that agree better with the previous experimental measurements than the homogeneous model relative permeability values. This is because the aggregate effect of the multiphase heterogeneities is to lower the core-average relative permeability of the fluid phases below that of relative permeability of any of the individual subdomains.

5.3 Darcy-Scale Models With Limited Permeability Information

To emphasize that exact experimental permeability measurements are not necessary to accurately reproduce experimental saturation measurements, two heterogeneous simulation models of each core are shown in Figure 7. The bold lines illustrate the CMG models that utilized single-phase flow-through permeability measurements of 1635 mD and 763 mD permeability in Core 1 and Core 2, respectively. The thin lines illustrate CMG simulations with the same heterogeneous relative permeability and capillary pressure derived from the pore network models, but with homogeneous permeability values of 1000 mD in both core samples. The slice-average saturation profiles in the models with different permeability only become distinguishable from each at very low water fractional flow. These results highlight that under the experimental conditions of this study, the saturation distributions are more sensitive to accurate capillary pressure characterization than to permeability parameterization.

6 Discussion and Implications

The characterization workflow proposed in this study opens the possibility for a digital workflow for estimating multiphase flow properties. In this workflow the most laborious components of a core analysis work program—such as core flooding relative permeability measurements—are no longer required. This is because the workflow utilizes only micro-CT images of dry cores, an independent measurement of porosity near the sample inlet (medical CT), a MICP curve, and some knowledge—from literature or experimental measurements—of the wettability and interfacial tension of the fluids in the system. The Darcy-scale model parameterized with heterogeneous PNM capillary pressure and relative permeability curves successfully captured subtle features of experimental observations and provided a more accurate match to the experimental saturation data at every fractional flow than the homogeneous models neglecting capillary heterogeneity.

The capillary pressure heterogeneity is the dominant mechanism controlling whole-core equivalent relative permeability and sub-core fluid saturation distribution at the cen-

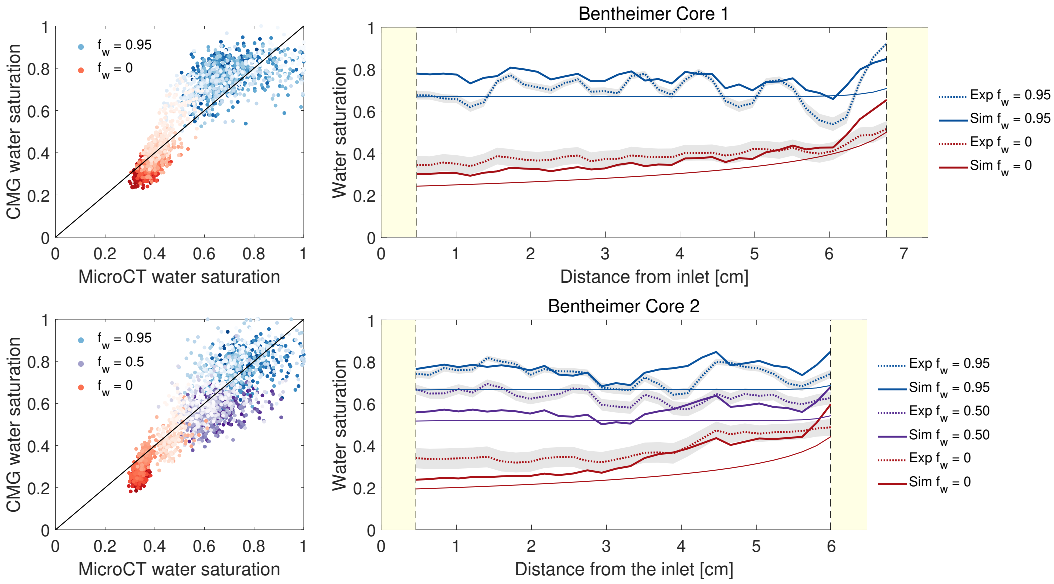

Figure 5. Water saturation comparison between multiscale simulation predictions and experimental measurements for Core 1 (top plots), and Core 2 (bottom plots). The figures on the left illustrate direct micro-CT subdomain to simulation grid cell comparison. The color darkness corresponds to the length along the core (e.g. dark red is near inlet and faint red is near the outlet). The figures on the right indicate the slice average saturations measured experimentally (dashed lines) and in the simulations (solid lines). The shaded gray region around the dashed lines indicates the saturation measurement uncertainty as described in the image processing workflow shown in Figure 2. The thick solid lines illustrate simulation results using heterogeneous capillary pressure and relative permeability input. The thin solid lines illustrate the homogeneous simulation model results. The experimental saturation profile in Core 2 indicates how the capillary barrier limits drainage on the downstream side of the barrier, leading to an increase in water saturation approximately 4 cm from the inlet of the core. Note the ability of the heterogeneous simulation model to capture this feature, particularly at a water fractional flow of zero (see Figure 1 for center-slice saturation comparison). Water fractional flows (f_w) of 0.95, 0.5, and 0 are respectively represented by blue, purple, and red in all plots. The vertical dashed lines and the shaded yellow regions in the plots on the right indicate the unscanned portion of the cores. The plots are different length because they are drawn on equal identical length scales but the cores have slightly different lengths.

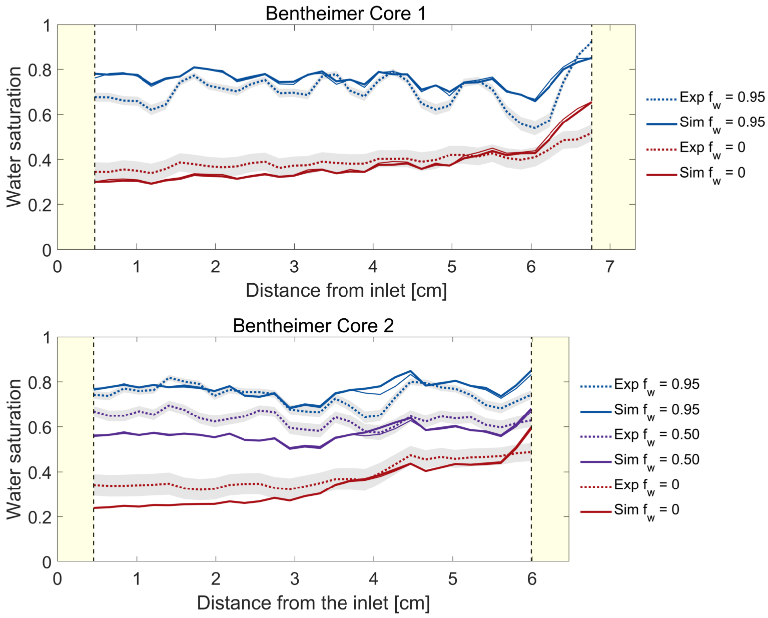

Figure 6. Water saturation slice-average profile comparison between simulation models with homogeneous and heterogeneous relative permeability compared with experimental measurements for Core 1 and Core 2. The thick solid lines are the simulations with heterogeneous PNM-derived relative permeability and capillary pressure curves assigned to each grid cell. These are identical to the lines shown in Figure 5. The thin solid lines are simulations in each core using the mean PNM relative permeability (bold colored lines in lower plot in Figure 3) but the same heterogeneous capillary pressure curves as the model indicated by the bold solid lines. Note that the solid thin lines and the solid thick lines are nearly indistinguishable at every fractional flow. The dashed lines are the slice-average saturations measured experimentally. The vertical dashed lines and the shaded yellow regions in the plots on the right indicate the unscanned portion of the cores.

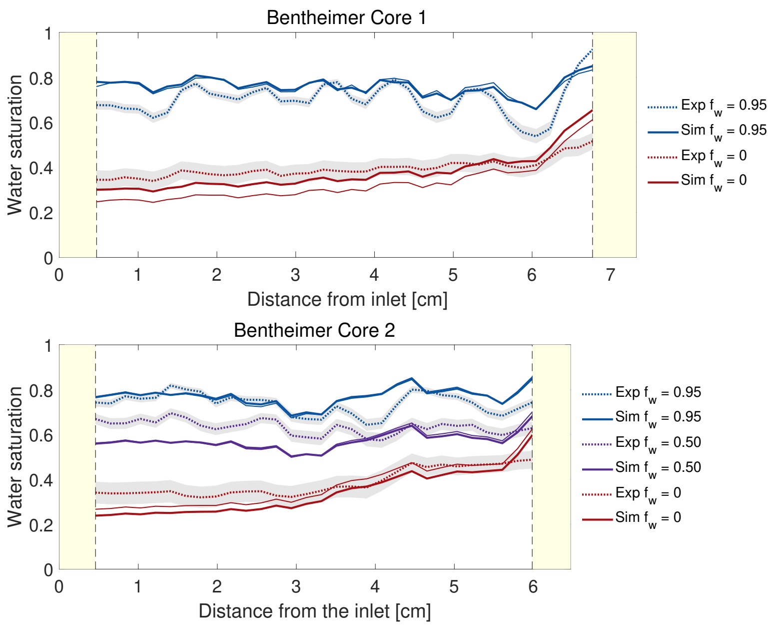

Figure 7. Water saturation slice-average profile comparison between simulation models and experimental measurements for Core 1 and Core 2. The dashed lines are the slice-average saturations measured experimentally and the thick solid lines are the simulations with 1635 mD and 763 mD permeability in Core 1 and Core 2, respectively. These are identical to the lines shown in Figure 5. The thin solid lines are simulations in each core using 1000 mD homogeneous permeability but the same heterogenous characteristic curves as the model indicated by the bold solid lines. Note that at high water fractional flow the solid lines are nearly indistinguishable. The shaded gray region around the dashed lines indicates the saturation measurement uncertainty. The vertical dashed lines and the shaded yellow regions in the plots on the right indicate the unscanned portion of the cores.

timeter length scale as shown in Figure 6. This may be in part because there is clear spatial structure to the heterogeneity in capillary pressure whereas heterogeneity in relative permeability characteristics are randomly distributed. However, the exact relative permeability structure cannot be conclusively determined without further investigation.

The importance of capillary heterogeneity is significant for a number of reasons. As demonstrated by the sensitivity analysis (Figure S2 in the SI), pore network model descriptions of capillary pressure are much less dependent on image processing uncertainty than relative permeability. This is also significant because sub-core scale estimates of capillary pressure characteristics can be validated by ganglia-curvature based measurements (Herring et al., 2017; Garing et al., 2017; Lin et al., 2018, 2018; Jackson et al., 2019), whereas estimates of relative permeability across similar size domains cannot.

The insensitivity of saturation distributions to absolute permeability demonstrated in Figure 7 indicates that this workflow does not require exact permeability measurements, but permeability could instead be approximated from literature values, relevant porosity-permeability relationships (Tiab & Donaldson, 2016), or possibly pore network modeling. While the pore network model output could be used to define the Darcy-scale permeability, the uncertainty analysis performed here agrees with previous studies that found permeability is highly sensitive to image processing (Beckingham et al., 2013; Guan et al., 2018). Conceptually this is because permeability calculations in pore network models are dominated by smallest throats along the flow path, and thus are very uncertain without model calibration. These observations agree with other work demonstrating the importance of capillary pressure characterization rather than permeability characterization for accurate multiphase flow modeling at low capillary numbers (Corbett et al., 1992; Krause, 2012; B. Li & Benson, 2015; Jackson, Mayachita, & Krevor, 2018).

We highlight that the capillary pressure of sample subdomains can be determined from image characterization of the capillary entry pressure. While the maximal ball method implemented in the PNextract open-source network extraction algorithm was used in this study, any number of open-source or commercial geometric or pore-scale modeling approaches could be used to estimate capillary entry pressure. The uncertainty analysis and simulation results indicate that pore network model capillary entry pressure estimates are accurate and relatively insulated from the image processing decisions because these measurements are based on the largest pore features in the images. When compared with the magnitude of a relatively subtle capillary barrier in the Bentheimer sandstone Core 2, the increase in capillary entry pressure in this feature was clearly differentiable from the bounds of image processing uncertainty.

Pore network modeling has several technical and practical advantageous over traditional multiphase flow characterization approaches. First, traditional approaches are impacted by experimental artifacts, such as the capillary end effects, as described in detail in Figure 3. Another advantage of using PNM to characterize capillary heterogeneity is that measurements are not influenced by viscous forces that are typically ignored with assumptions of capillary equilibrium across the system (Krause et al., 2013; Pini & Benson, 2013, 2017; Jackson, Agada, et al., 2018; Hejazi et al., 2019). Finally, approaches for quantifying capillary heterogeneity rely on J-Leverett scaling (Leverett, 1940; Krause et al., 2013; Pini & Benson, 2013). This scaling assumes that the relationship between local capillary pressure, porosity, and permeability are fixed for a given sample (often referred to as the J-function). While these assumptions have been rigorously tested in sandstones, they are likely to break down in more complex reservoir types such as carbonates and non-sedimentary systems. In circumventing the need for these types of assumptions—along with expensive and time-consuming experimental characterization—this digital pore network model approach mitigates key practical barriers to incorporating small-scale capillary heterogeneity into reservoir simulation upscaling workflows. This approach is therefore applicable in more highly heterogeneous rocks as long as the REV is not larger than the size of the sample than can be scanned with micro-CT (1.24 cm diameter with the scanner used in this study).

It is important to reemphasize that the multiphase simulation model input presented and compared with the experimental data was sourced from an uncalibrated pore network model, assuming some knowledge of fluid contact angle and interfacial tension. As a result of this calibration-free approach, we have illustrated a predictive multiscale characterization workflow. This work provides a new way to rapidly estimate characteristic relative permeability and drainage capillary pressure data without the need for flow-through experiments. Future work is needed to test these approaches for imbibition capillary pressure curve characterization. More rapid and economical characterization will significantly improve numerical models of complex fluid flow processes in the subsurface. Improved multiphase models are essential for better predictions of complex multiphase flow problems such as global-scale carbon mitigation with geologic carbon sequestration, contaminate migration and remediation, and invasion of pollutants into the vadose zone.

Acknowledgments

Supplemental data is available on the British Geological Survey National Geoscience Data Centre at doi.org/10.5285/4483646c-6e21-4927-a2bf-60f9648e6dec.

Funding for this work was provided by ACT ELEGANCY, Project No 271498, has received funding from DETEC (CH), BMWi (DE), RVO (NL), Gassnova (NO), BEIS (UK), Gassco, Equinor and Total, and is cofunded by the European Commission under the Horizon 2020 programme, ACT Grant Agreement No 691712. Samuel Jackson received funding from the Natural Environment Research Council, Grant number: NE/N016173/1. The authors wish to thank five reviewers for their valuable comments and feedback.

References

Akin, S., & Kovscek, A. (2003). Computed Tomography in Petroleum Engineering Research. *Applications of X-ray Computed Tomography in the Geosciences*, *215*, 23–38.

Al-Khulaifi, Y., Lin, Q., Blunt, M. J., & Bijeljic, B. (2019). Pore-Scale Dissolution by CO2 Saturated Brine in a Multimineral Carbonate at Reservoir Conditions: Impact of Physical and Chemical Heterogeneity. *Water Resources Research*, *55*(4), 3171–3193. doi: 10.1029/2018WR024137

Al-Menhali, A. S., & Krevor, S. (2016). Capillary Trapping of CO2 in Oil Reservoirs: Observations in a Mixed-Wet Carbonate Rock. *Environmental Science and Technology*, *50*(5), 2727–2734. doi: 10.1021/acs.est.5b05925

Armstrong, R. T., Porter, M. L., & Wildenschild, D. (2012). Linking pore-scale interfacial curvature to column-scale capillary pressure. *Advances in Water Resources*, *46*, 55–62. Retrieved from `http://dx.doi.org/10.1016/j.advwatres.2012.05.009` doi: 10.1016/j.advwatres.2012.05.009

Arns, C. H., Knackstedt, M. A., Pinczewski, W. V., & Lindquist, W. B. (2001). Accurate estimation of transport properties from microtomographic images. *Geophysics Research Letters*, *28*(17), 3361–3364.

Bakke, S., & Øren, P.-E. (1997). 3-D Pore-Scale Modelling of Sandstones and Flow Simulations in the Pore Networks. *SPE Journal*, *2*(02), 136–149. doi: 10.2118/35479-pa

Bartels, W., Rücker, M., Boone, M., Bultreys, T., Mahani, H., Berg, S., … Cnudde, V. (2019). Imaging spontaneous imbibition in full Darcyscale samples at porescale resolution by fast Xray tomography. *Water Resources Research*, *Accepted*, 1–29. Retrieved from `https://onlinelibrary.wiley.com/doi/abs/10.1029/2018WR024541` doi: 10.1029/2018WR024541

Beckingham, L. E., Peters, C. A., Um, W., Jones, K. W., & Lindquist, W. B. (2013). 2D and 3D imaging resolution trade-offs in quantifying pore throats for prediction of permeability. *Advances in Water Resources*, *62*, 1–12. doi: 10.1016/j.advwatres.2013.08.010

Beckingham, L. E., Steefel, C. I., Swift, A. M., Voltolini, M., Yang, L., Anovitz, L. M., … Xue, Z. (2017). Evaluation of accessible mineral surface areas for improved prediction of mineral reaction rates in porous media. *Geochimica et*

Cosmochimica Acta, *205*, 31–49. doi: 10.1016/j.gca.2017.02.006

Berg, S., Rücker, M., Ott, H., Georgiadis, A., van der Linde, H., Enzmann, F., ... Wiegmann, A. (2016). Connected pathway relative permeability from pore-scale imaging of imbibition. *Advances in Water Resources*, *90*, 24–35. doi: 10.1016/j.advwatres.2016.01.010

Berg, S., Saxena, N., Shaik, M., & Pradhan, C. (2018). Generation of ground truth images to validate micro-CT image-processing pipelines. *The Leading Edge*, *37*(6), 412–420. doi: 10.1190/tle37060412.1

Bijeljic, B., Muggeridge, A. H., & Blunt, M. J. (2004). Pore-scale modeling of longitudinal dispersion. *Water Resources Research*, *40*(11), 1–9. doi: 10.1029/2004WR003567

Blunt, M., & King, P. (1991). Relative Permeabilities from Two-and Three-Dimensional Pore-Scale Network Modelling. *Transport in Porous Media*, *6*, 407–433. Retrieved from `https://link.springer.com/content/pdf/10.1007{\%}2FBF00136349.pdf`

Blunt, M. J. (1997). *Effects of Heterogeneity and Wetting on Relative Permeability Using Pore Level Modeling* (Vol. 2). doi: SPE36762

Buades, A., Coll, B., & Morel, J. M. (2005). A non-local algorithm for image denoising. *Proceedings - 2005 IEEE Computer Society Conference on Computer Vision and Pattern Recognition, CVPR 2005*, *II*(0), 60–65. doi: 10.1109/CVPR.2005.38

Bultreys, T., De Boever, W., & Cnudde, V. (2016). Imaging and image-based fluid transport modeling at the pore scale in geological materials: A practical introduction to the current state-of-the-art. *Earth-Science Reviews*, *155*, 93–128. Retrieved from `http://dx.doi.org/10.1016/j.earscirev.2016.02.001` doi: 10.1016/j.earscirev.2016.02.001

Bultreys, T., Lin, Q., Gao, Y., Raeini, A. Q., Alratrout, A., Bijeljic, B., & Blunt, M. J. (2018). Validation of model predictions of pore-scale fluid distributions during two-phase flow. *Physical Review E*, *97*(5). doi: 10.1103/PhysRevE.97.053104

Chaudhary, K., Bayani Cardenas, M., Wolfe, W. W., Maisano, J. A., Ketcham, R. A., & Bennett, P. C. (2013). Pore-scale trapping of supercritical CO2 and the role of grain wettability and shape. *Geophysical Research Letters*, *40*(15), 3878–3882. doi: 10.1002/grl.50658

Chen, J. D., & Wilkinson, D. (1985). Pore-scale viscous fingering in porous media. *Physical Review Letters*, *55*(18), 1892–1895. doi: 10.1103/PhysRevLett.55.1892

Computer Modelling Group LTD. (2017). *IMEX Three-phase, Black-oil Reservoir Simulator.* Calgary, Alberta Canada: Computer Modelling Group LTD.

Corbett, P. W. M., Ringrose, P. S., Jensen, J. L., & Sorbie, K. S. (1992). Laminated clastic reservoirs: The interplay of capillary pressure and sedimentary architecture. *Proceedings - SPE Annual Technical Conference and Exhibition*, 365–376.

Cowton, L. R., Neufeld, J. A., White, N. J., Bickle, M. J., Williams, G. A., White, J. C., & Chadwick, R. A. (2018). Benchmarking of vertically-integrated CO2 flow simulations at the Sleipner Field, North Sea. *Earth and Planetary Science Letters*, *491*, 121–133. Retrieved from `https://doi.org/10.1016/j.epsl.2018.03.038` doi: 10.1016/j.epsl.2018.03.038

De Chalendar, J. A., Garing, C., & Benson, S. M. (2018). Pore-scale modelling of Ostwald ripening. *Journal of Fluid Mechanics*, *835*, 363–392. doi: 10.1017/jfm.2017.720

Dong, H., & Blunt, M. J. (2009). Pore-network extraction from micro-computerized-tomography images. *Physical Review E*, *80*(3), 036307. Retrieved from `https://link.aps.org/doi/10.1103/PhysRevE.80.036307` doi: 10.1103/PhysRevE.80.036307

Eiken, O., Ringrose, P., Hermanrud, C., Nazarian, B., Torp, T. A., & Høier, L. (2011). Lessons Learned from 14 years of CCS Operations: Sleipner, In Salah and Snøhvit. *Energy Procedia*, *4*, 5541–5548. doi: 10.1016/j.egypro.2011.02.541

Espinoza, D. N., & Santamarina, J. C. (2010). Water-CO2-mineral systems: Interfacial tension, contact angle, and diffusionImplications to CO2 geological storage. *Water Resources Research*, *46*(7), 1–10. doi: 10.1029/2009WR008634

Ethington, E. F. (1990). *Interfacial contact angle measurements of water, mercury, and 20 organic liquids on quartz, calcite, biotite, and Ca-montmorillonite substrates* (Tech. Rep. No. July). doi: 10.1016/j.conbuildmat.2005.09.001

Feehley, C. E., Zheng, C., & Molz, F. J. (2000). A dual-domain mass transfer approach for modeling solute transport in heterogeneous aquifers: Application to the macrodispersion experiment (MADE) site. *Water Resources Research*, *36*(9), 2501–2515. doi: 10.1029/2000WR900148

Garing, C., de Chalendar, J. A., Voltolini, M., Ajo-Franklin, J. B., & Benson, S. M. (2017). Pore-scale capillary pressure analysis using multi-scale X-ray micromotography. *Advances in Water Resources*, *104*, 223–241. Retrieved from `http://dx.doi.org/10.1016/j.advwatres.2017.04.006` doi: 10.1016/j.advwatres.2017.04.006

Guan, K. M., Guo, B., Creux, P., Kovscek, A. R., Tchelepi, H., & Nazarova, M. (2018). Effects of Image Resolution on Sandstone Porosity and Permeability as Obtained from X-Ray Microscopy. *Transport in Porous Media*, *127*(1), 233–245. Retrieved from `https://doi.org/10.1007/s11242-018-1189-9` doi: 10.1007/s11242-018-1189-9

Guice, K., Lun, L., Gao, B., Gupta, R., Gupta, G., Kralik, J. G., . . . Jawhari, A. (2014). An Evaluation of Digital Rock Physics Technology for the Prediction of Relative Permeability and Capillary Pressure for a Middle Eastern Carbonate Reservoir. *International Petroleum Technology Conference*, *IPTC 17288*, 1–11.

Halisch, M. (2013). The Rev Challenge Estimating Representative Elementary Volumes and Porous Rock Inhomogeneity From High Resolution Micro-Ct Data Sets. *Society of Core Analysts*(069), 1–7.

Hejazi, S. A. H., Shah, S., & Pini, R. (2019). Dynamic measurements of drainage capillary pressure curves in carbonate rocks. *Chemical Engineering Science*, *200*, 268–284. Retrieved from `https://www.sciencedirect.com/science/article/pii/S0009250919301356?via{\%}3Dihub` doi: 10.1016/J.CES.2019.02.002

Herring, A. L., Harper, E. J., Andersson, L., Sheppard, A., Bay, B. K., & Wildenschild, D. (2013). Effect of fluid topology on residual nonwetting phase trapping: Implications for geologic CO2 sequestration. *Advances in Water Resources*, *62*, 47–58. Retrieved from `http://dx.doi.org/10.1016/j.advwatres.2013.09.015` doi: 10.1016/j.advwatres.2013.09.015

Herring, A. L., Middleton, J., Walsh, R., Kingston, A., & Sheppard, A. (2017). Flow rate impacts on capillary pressure and interface curvature of connected and disconnected fluid phases during multiphase flow in sandstone. *Advances in Water Resources*, *107*, 460–469. Retrieved from `http://dx.doi.org/10.1016/j.advwatres.2017.05.011` doi: 10.1016/j.advwatres.2017.05.011

Hilpert, M., & Miller, C. T. (2001). Pore-morphology-based simulation of drainage in totally wetting porous media. *Advances in Water Resources*, *24*(3-4), 243–255. doi: 10.1016/S0309-1708(00)00056-7

Hussain, F., Pinczewski, W. V., Cinar, Y., Arns, J. Y., Arns, C. H., & Turner, M. L. (2014). Computation of Relative Permeability from Imaged Fluid Distributions at the Pore Scale. *Transport in Porous Media*, *104*(1), 91–107. doi: 10.1007/s11242-014-0322-7

Idowu, N. A., & Blunt, M. J. (2010). Pore-scale modelling of rate effects in waterflooding. *Transport in Porous Media*, *83*(1), 151–169. doi: 10.1007/s11242-009-9468-0

Iglauer, S., Fernø, M. A., Shearing, P., & Blunt, M. J. (2012). Comparison of residual oil cluster size distribution, morphology and saturation in oil-wet and water-wet sandstone. *Journal of Colloid and Interface Science*, *375*(1), 187–192. Retrieved from `http://dx.doi.org/10.1016/j.jcis.2012.02.025` doi: 10.1016/j.jcis.2012.02.025

Jackson, S. J., Agada, S., Reynolds, C. A., & Krevor, S. (2018). Characterizing Drainage Multiphase Flow in Heterogeneous Sandstones. *Water Resources Research*, *54*(4), 3139–3161. doi: 10.1029/2017WR022282

Jackson, S. J., Lin, Q., & Krevor, S. (2019). Representative elementary volumes, hysteresis and heterogeneity in multiphase flow from the pore to continuum scale. *Submitted and available on EarthArXiv*(22 September), 1–33. Retrieved from `https://eartharxiv.org/2aejr/`

Jackson, S. J., Mayachita, I., & Krevor, S. (2018). High resolution modelling and steady-state upscaling of large scale gravity currents in heterogeneous sandstone reservoirs. *5th CO2 Geological Storage Workshop*, *2018-Novem*(November 2018).

Jerauld, G. R., & Salter, S. J. (1990). The Effect of Pore Structure on Hysteresis in Relative Permeability and Capillary Pressure: Pore Level Modeling. *Transport in Porous Media*, *5*, 103.

Jiang, Z., Wu, K., Couples, G., Van Dijke, M. I., Sorbie, K. S., & Ma, J. (2007). Efficient extraction of networks from three-dimensional porous media. *Water Resources Research*, *43*(12), 1–17. doi: 10.1029/2006WR005780

Joekar-Niasar, V., Prodanović, M., Wildenschild, D., & Hassanizadeh, S. M. (2010). Network model investigation of interfacial area, capillary pressure and saturation relationships in granular porous media. *Water Resources Research*, *46*(6), 1–18. doi: 10.1029/2009WR008585

Kang, P. K., Lee, J., Fu, X., Lee, S., Peter K. Kitanidis, & Juanes, R. (2017). Improved characterization of heterogeneous permeability in saline aquifers from transient pressure data during freshwater injection. *Water Resources Research*, *53*, 4444–4458. doi: 10.1002/2016WR020089.Received

Kazakov, A., Muzny, C. D., Kroenlein, K., Diky, V., Chirico, R. D., Magee, J. W., ... Frenkel, M. (2012). NIST/TRC source data archival system: The next-generation data model for storage of thermophysical properties. *International Journal of Thermophysics*, *33*(1), 22–33. doi: 10.1007/s10765-011-1107-7

Krause, M. (2012). Modeling and investigation of the influence of capillary heterogeneity on relative permeability. *SPE Annual Technical Conference and Exhibition*(October), 8–10. Retrieved from https://www.onepetro.org/conference-paper/SPE-160909-STU

Krause, M., Krevor, S., & Benson, S. M. (2013). A Procedure for the Accurate Determination of Sub-Core Scale Permeability Distributions with Error Quantification. *Transport in Porous Media*, *98*(3), 565–588.

Krevor, S. C. M., Pini, R., Li, B., & Benson, S. M. (2011, aug). Capillary heterogeneity trapping of CO2 in a sandstone rock at reservoir conditions. *Geophysical Research Letters*, *38*(15), n/a–n/a. Retrieved from http://doi.wiley.com/10.1029/2011GL048239 doi: 10.1029/2011GL048239

Lai, P., Moulton, K., & Krevor, S. (2015). Pore-scale heterogeneity in the mineral distribution and reactive surface area of porous rocks. *Chemical Geology*, *411*, 260–273. Retrieved from http://dx.doi.org/10.1016/j.chemgeo.2015.07.010 doi: 10.1016/j.chemgeo.2015.07.010

Lenormand, R., Touboul, E., & Zarcone, C. (1988). NUmerical models and experiments on immiscible discplacements in porous media. *Journal of Fluid Mechanics*, *189*(C), 165–187. Retrieved from papers3://publication/uuid/500C8DAA-9E14-45CC-A2EF-5CCBEA82D161

Leu, L., Berg, S., Enzmann, F., Armstrong, R. T., & Kersten, M. (2014). Fast X-ray Micro-Tomography of Multiphase Flow in Berea Sandstone: A Sensitivity Study on Image Processing. *Transport in Porous Media*, *105*(2), 451–469. doi: 10.1007/s11242-014-0378-4

Leverett, M. (1940). Capillary Behavior in Porous Solids. *Petroleum Technology*, *August*, 152–169.

Li, B., & Benson, S. M. (2015). Influence of small-scale heterogeneity on upward CO2 plume migration in storage aquifers. *Advances in Water Resources*, *83*, 389–404. doi: 10.1016/j.advwatres.2015.07.010

Li, J., McDougall, S. R., & Sorbie, K. S. (2017). Dynamic pore-scale network model (PNM) of water imbibition in porous media. *Advances in Water Resources*, *107*, 191–211. doi: 10.1016/j.advwatres.2017.06.017

Li, T., Schlüter, S., Dragila, M. I., & Wildenschild, D. (2018). An improved method for estimating capillary pressure from 3D microtomography images and its application to the study of disconnected nonwetting phase. *Advances in Water Resources*, *114*, 249–260. Retrieved from `https://doi.org/10.1016/j.advwatres.2018.02.012` doi: 10.1016/j.advwatres.2018.02.012

Lin, Q., Al-Khulaifi, Y., Blunt, M. J., & Bijeljic, B. (2016). Quantification of sub-resolution porosity in carbonate rocks by applying high-salinity contrast brine using X-ray microtomography differential imaging. *Advances in Water Resources*, *96*, 306–322. doi: 10.1016/j.advwatres.2016.08.002

Lin, Q., Bijeljic, B., Berg, S., Pini, R., Blunt, M. J., & Krevor, S. (2019). Minimal surfaces in porous media: Pore-scale imaging of multiphase flow in an altered-wettability Bentheimer sandstone. *Physical Review E*, *99*(6), 1–13. doi: 10.1103/PhysRevE.99.063105

Lin, Q., Bijeljic, B., Pini, R., Blunt, M. J., & Krevor, S. (2018). Imaging and measurement of pore-scale interfacial curvature to determine capillary pressure simultaneously with relative permeability. *Water Resources Research*, 7046–7060. Retrieved from `http://doi.wiley.com/10.1029/2018WR023214` doi: 10.1029/2018WR023214

Lindquist, W. B., Coker, D. A., Spanne, P., Lee, S.-M., & Jones, K. W. (2004). Medial axis analysis of void structure in three-dimensional tomographic images of porous media. *Journal of Geophysical Research: Solid Earth*, *101*(B4), 8297–8310. doi: 10.1029/95jb03039

Mason, G., & Morrow, N. R. (1991). Capillary behavior of a perfectly wetting liquid in irregular triangular tubes. *Journal of Colloid And Interface Science*, *141* (1), 262–274. doi: 10.1016/0021-9797(91)90321-X

Mehmani, Y., & Tchelepi, H. A. (2017). Minimum requirements for predictive pore-network modeling of solute transport in micromodels. *Advances in Water Resources*, *108*, 83–98. Retrieved from https://doi.org/10.1016/j.advwatres.2017.07.014 doi: 10.1016/j.advwatres.2017.07.014

Menke, H. P., Bijeljic, B., Andrew, M. G., & Blunt, M. J. (2015). Dynamic three-dimensional pore-scale imaging of reaction in a carbonate at reservoir conditions. *Environmental Science and Technology*, *49* (7), 4407–4414. doi: 10.1021/es505789f

Nguyen, V. H., Sheppard, A. P., Knackstedt, M. A., & Val Pinczewski, W. (2006). The effect of displacement rate on imbibition relative permeability and residual saturation. *Journal of Petroleum Science and Engineering*, *52* (1-4), 54–70. doi: 10.1016/j.petrol.2006.03.020

Norton, D., & Knapp, R. (1977). Transport phenomena in hydrothermal systems: The nature of porosity. *American Journal of Science*, *277*, 913–936. Retrieved from papers2://publication/uuid/F03A8A4C-B5FD-4004-8493-CBFA884B7133

Øren, P. E., Ruspini, L. C., Saadatfar, M., Sok, R. M., Knackstedt, M., & Herring, A. (2019). In-situ pore-scale imaging and image-based modelling of capillary trapping for geological storage of CO 2 International Journal of Greenhouse Gas Control In-situ pore-scale imaging and image-based modelling of capillary trapping for geological storage of . *International Journal of Greenhouse Gas Control*, *87*(May), 34–43. Retrieved from https://doi.org/10.1016/j.ijggc.2019.04.017 doi: 10.1016/j.ijggc.2019.04.017

Papafotiou, A., Helmig, R., Schaap, J., Lehmann, P., Kaestner, A., Fluhler, H., . . . Durner, W. (2008). From the pore scale to the lab scale: 3-D lab experiment and numerical simulation of drainage in heterogeneous porous media. *Advances in Water Resources*, *31* (9), 1253–1268. doi: 10.1016/j.advwatres.2007.09.006

Pianosi, F., Beven, K., Freer, J., Hall, J. W., Rougier, J., Stephenson, D. B., & Wagener, T. (2016). Sensitivity analysis of environmental models: A systematic review with practical workflow. *Environmental Modelling and Software*, *79*, 214–232. Retrieved from `http://dx.doi.org/10.1016/j.envsoft.2016.02.008` doi: 10.1016/j.envsoft.2016.02.008

Pini, R., & Benson, S. M. (2013). Characterization and scaling of mesoscale heterogeneities in sandstones. *Geophysical Research Letters*, *40*(15), 3903–3908. doi: 10.1002/grl.50756

Pini, R., & Benson, S. M. (2017). Capillary pressure heterogeneity and hysteresis for the supercritical CO 2 /water system in a sandstone. *Advances in Water Resources*, *108*, 277–292. Retrieved from `http://linkinghub.elsevier.com/retrieve/pii/S0309170817304189` doi: 10.1016/j.advwatres.2017.08.011

Raeini, A. Q., Bijeljic, B., & Blunt, M. J. (2015). Modelling capillary trapping using finite-volume simulation of two-phase flow directly on micro-CT images. *Advances in Water Resources*, *83*, 102–110. Retrieved from `http://dx.doi.org/10.1016/j.advwatres.2015.05.008` doi: 10.1016/j.advwatres.2015.05.008

Raeini, A. Q., Bijeljic, B., & Blunt, M. J. (2017). Generalized network modeling: Network extraction as a coarse-scale discretization of the void space of porous media. *Physical Review E*, *96*(1), 1–17. doi: 10.1103/PhysRevE.96.013312

Raeini, A. Q., Bijeljic, B., & Blunt, M. J. (2018). Generalized network modeling of capillary-dominated two-phase flow. *Physical Review E*, *97*(2). doi: 10.1103/PhysRevE.97.023308

Raeini, A. Q., Yang, J., Bondino, I., Bultreys, T., Blunt, M. J., & Bijeljic, B. (2019). Validating the Generalized Pore Network Model Using Micro-CT Images of Two-Phase Flow. *Transport in Porous Media*. Retrieved from `http://link.springer.com/10.1007/s11242-019-01317-8` doi: 10.1007/s11242-019-01317-8

Rajaram, H., Ferrand, L. A., & Celia, M. A. (1997). Prediction of relative permeabilities for unconsolidated soils using pore-scale network models. *Water Resources Research*, *33*(1), 43–52. doi: 10.1029/96WR02841

Reynolds, C. A., Blunt, M. J., & Krevor, S. (2018). Multiphase Flow Characteristics of Heterogeneous Rocks From CO2 Storage Reservoirs in the United Kingdom. *Water Resources Research*, *54*, 729–745. Retrieved from `http://doi.wiley.com/10.1002/2017WR021651` doi: 10.1002/2017WR021651

Reynolds, C. A., & Krevor, S. (2015). Characterizing flow behavior for gas injection: Relative permeability of CO2-brine and N2-water in heterogeneous rocks. *Water Resources Research*, *50*, 9464–9489. doi: 10.1002/2015WR017273.Received

Reynolds, C. A., Menke, H., Andrew, M., Blunt, M. J., & Krevor, S. (2017). Dynamic fluid connectivity during steady-state multiphase flow in a sandstone. *Proceedings of the National Academy of Sciences*, *114*(31), 8187–8192. Retrieved from `http://www.pnas.org/lookup/doi/10.1073/pnas.1702834114` doi: 10.1073/pnas.1702834114

Ringrose, P., Atbi, M., Mason, D., Espinassous, M., Myhrer, b., Myhrer, Ø., ... Wright, I. (2009). Plume development around well KB-502 at the In Salah CO2 storage site. *First Break*, *27*(7005), 85–89. Retrieved from `http://www.earth.uwaterloo.ca/graduate/courses/earth691-duss/CO2{\_}GeneralCO2Sequestrationmaterilas/CO2{\_}FBJan09{\_}spectop5-1.pdf`

Ringrose, P. S., Sorbie, K. S., Corbett, P. W. M., & Jensen, J. L. (1993). Immiscible flow behaviour in laminated and cross-bedded sandstones. *Journal of Petroleum Science and Engineering*, *9*(2), 103–124. doi: 10.1016/0920-4105(93)90071-L

Sage, D., Prodanov, D., Tinevez, J.-Y., & Schindelin, J. (2012). MIJ: Making Interoperability Between ImageJ and Matlab Possible. In *Imagej user & developer conference.* Luxembourg.

Sheng, Q., & Thompson, K. (2016). A unified pore-network algorithm for dynamic two-phase flow. *Advances in Water Resources*, *95*, 92–108. Retrieved from `http://dx.doi.org/10.1016/j.advwatres.2015.12.010` doi: 10.1016/j.advwatres.2015.12.010

Silin, D., & Patzek, T. (2006). Pore space morphology analysis using maximal inscribed spheres. *Physica A: Statistical Mechanics and its Applications*, *371*(2), 336–360. doi: 10.1016/j.physa.2006.04.048

Singh, A., Armstrong, R., Regenauer-Lieb, K., & Mostaghimi, P. (2018). Rock characterization using Gray-Level Co-occurrence Matrix: An objective perspective of digital rock statistics. *Water Resources Research*(2009). doi: 10.1029/2018wr023342

Singh, V., Cavanagh, A., Hansen, H., Nazarian, B., Iding, M., & Ringrose, P. (2010).

Reservoir modeling of CO2 plume behavior calibrated against monitoring data from sleipner, Norway. *Proceedings - SPE Annual Technical Conference and Exhibition*, *5*, 3461–3479.

Tiab, D., & Donaldson, E. C. (2016). Porosity and Permeability. In *Petrophysics -theory and practice of measuring reservoir rock and fluid transport properties* (4th ed., pp. 67–186). San Francisco: Elsevier. Retrieved from http://linkinghub.elsevier.com/retrieve/pii/B978012397021300017X doi: 10.1016/B978-0-12-397021-3.00017-X

Valvatne, P. H., & Blunt, M. J. (2004). Predictive pore-scale modeling of two-phase flow in mixed wet media. *Water Resources Research*, *40*(7), 1–21. doi: 10.1029/2003WR002627

Vogel, H.-J., Tölke, J., Schulz, V. P., Krafczyk, M., & Roth, K. (2005). Comparison of a Lattice-Boltzmann Model, a Full-Morphology Model, and a Pore Network Model for Determining Capillary PressureSaturation Relationships. *Vadose Zone Journal*, *4*(2), 380. doi: 10.2136/vzj2004.0114

Wildenschild, D., & Sheppard, A. P. (2013). X-ray imaging and analysis techniques for quantifying pore-scale structure and processes in subsurface porous medium systems. *Advances in Water Resources*, *51*, 217–246. Retrieved from http://dx.doi.org/10.1016/j.advwatres.2012.07.018 doi: 10.1016/j.advwatres.2012.07.018

Zahasky, C., & Benson, S. M. (2018). Micro-Positron Emission Tomography for Measuring Sub-core Scale Single and Multiphase Transport Parameters in Porous Media. *Advances in Water Resources*, *115*, 1–16. Retrieved from http://linkinghub.elsevier.com/retrieve/pii/S030917081731182X doi: 10.1016/j.advwatres.2018.03.002

Zahasky, C., Thomas, D., Matter, J., Maher, K., & Benson, S. M. (2018). Multimodal imaging and stochastic percolation simulation for improved quantification of effective porosity and surface area in vesicular basalt. *Advances in Water Resources*, *121*(June), 235–244. Retrieved from https://doi.org/10.1016/j.advwatres.2018.08.009 doi: 10.1016/j.advwatres.2018.08.009

Zhao, B., MacMinn, C. W., Primkulov, B. K., Chen, Y., Valocchi, A. J., Zhao, J., … Juanes, R. (2019). Comprehensive comparison of pore-scale models for multiphase flow in porous media. *Proceedings of the National Academy* *of Sciences of the United States of America*, *116*(28), 13799–13806. doi: 10.1073/pnas.1901619116